



In-situ imaging of heat-induced phase transition in a two-dimensional conjugated metal-organic framework

David Mücke^{a,b,*}, Baokun Liang^a, Zhiyong Wang^{c,d,**}, Haoyuan Qi^a, Renhao Dong^{c,e}, Xinliang Feng^{c,d}, Ute Kaiser^{a,b,*}

^a Central Facility for Materials Science Electron Microscopy, Universität Ulm, Ulm 89081, Germany

^b Institute for Quantum Optics, Universität Ulm, Ulm 89081, Germany

^c Faculty of Chemistry and Food Chemistry & Center for Advancing Electronics Dresden (cfaed), Technische Universität Dresden, Dresden 01062, Germany

^d Max Planck Institute of Microstructure Physics, Halle (Saale) 06120, Germany

^e Key Laboratory of Colloid and Interface Chemistry of the Ministry of Education, School of Chemistry and Chemical Engineering, Shandong University, Jinan 250100, China

ARTICLE INFO

Keywords:

HRTEM

in-situ

Metal-organic frameworks

Heating

Phase transition

ABSTRACT

Atomically-resolved in-situ high-resolution transmission electron microscopy (HRTEM) imaging of the structural dynamics in organic materials remains a major challenge. This difficulty persists even with aberration-corrected instruments, as HRTEM images necessitate a high electron dose that is generally intolerable for organic materials. In this study, we report the in-situ HRTEM imaging of heat-induced structural dynamics in a benzenehexathiol-based two-dimensional conjugated metal-organic framework (2D c-MOF, i.e., Cu₃(BHT)). Leveraging its hydrogen-free structure and high electrical conductivity, Cu₃(BHT) exhibits high electron beam resistance. We demonstrate atomic resolution imaging at an 80 kV electron accelerating voltage using our Cc/Cs-corrected SALVE instrument. However, continuous electron irradiation eventually leads to its amorphization. Intriguingly, under heating in a MEMS holder, the Cu₃(BHT) undergoes a phase transition to a new crystalline phase and its phase transition, occurring within the temperature range of 480 °C to 620 °C in dependence on the electron beam illumination. Using HRTEM and energy-dispersive X-ray mapping, we identify this new phase as CuS. Our findings provide insights into the mechanisms governing structural transitions in purposefully engineered structures, potentially pivotal for future endeavours involving the production of metal oxide/sulfide nanoparticles from MOF precursors.

1. Introduction

Metal-organic frameworks (MOFs) represent an emerging class of crystalline porous materials constructed from metal-containing nodes and organic ligands (Dong et al., 2018; Huang et al., 2015). Due to their unique features, including a high degree of structural and chemical tailorability and high porosity, research on MOFs with alternating organic ligands, metal centers and framework geometries has increased dramatically, as has the number of potential applications, such as gas storage (Murray et al., 2009), separations (Li et al., 2012), and catalysis (Corma et al., 2010). In addition, MOFs are of growing interest for the production of nanoparticles (Chen et al., 2009; Negar et al., 2021;

Shahangi Shirazi and Akhbari, 2015; Zhang and Hu, 2010). Through thermal degradation of MOFs, nanoparticles of metal oxides (Negar et al., 2021; Shahangi Shirazi and Akhbari, 2015; Zhang and Hu, 2010) or metal chalcogenides (Luo et al., 2019) but also metal clusters (Chen et al., 2009) can be produced. CuS stands out as a p-type semiconductor with applications ranging from solar cells and chemical sensors to a large variety of other electrical applications (Saranya et al., 2014), depending on the size and morphology of the nanoparticle (Goel et al., 2014). However, the production of CuS by thermal degradation of MOFs differs significantly from other synthesis techniques such as hydrothermal/solvothermal methods, sonochemical synthesis or microwave irradiation (Goel et al., 2014). Despite rapid advances in synthesis and

* Corresponding authors at: Central Facility for Materials Science Electron Microscopy, Universität Ulm, Ulm 89081, Germany.

** Corresponding authors at: Faculty of Chemistry and Food Chemistry & Center for Advancing Electronics Dresden (cfaed), Technische Universität Dresden, Dresden 01062, Germany.

E-mail addresses: david.muecke@uni-ulm.de (D. Mücke), wang.zhiyong@tu-dresden.de (Z. Wang), ute.kaiser@uni-ulm.de (U. Kaiser).

<https://doi.org/10.1016/j.micron.2024.103677>

Received 19 April 2024; Received in revised form 6 June 2024; Accepted 7 June 2024

Available online 13 June 2024

0968-4328/© 2024 The Authors. Published by Elsevier Ltd. This is an open access article under the CC BY license (<http://creativecommons.org/licenses/by/4.0/>).

theory, the response of MOFs to external stimulation remains largely unexplored. As a result, the nanoparticle production via thermal degradation has not been explored so far. Recently, Bennett and co-workers have investigated the structural changes in the zeolitic imidazolate framework (ZIF) family of MOFs upon external stimuli such as high pressure and high temperature, showing structural collapses and transitions to liquid states, respectively (Widmer et al., 2019). Complex behavior in ZIF-62 and ZIF-4 were identified with distinct high- and low-density amorphous phases, existing in different regions of the pressure–temperature phase diagram. However, the structural evolution was monitored by *in-situ* powder X-ray diffraction, offering a spatially-averaged depiction of the transition process. To the best of our knowledge, there are no reports on atomic resolution real space investigations. Due to the lack of suitable methods for *in-situ* monitoring of the structural changes, there is also a lack of clarity regarding the processes involved in nanoparticle formation during heating. Aberration-corrected high-resolution transmission electron microscopy (AC-HRTEM) has been proven a powerful technique for revealing inorganic material structures *in-situ* with sub-angstrom (\AA) resolution at voltages ranging from 300 kV (Haider et al., 1998; Jia et al., 2014) down to 20 kV (Linck et al., 2016; Kaiser, 2024). The latter voltage was realized in the frame of the sub-Ångstrom low-voltage electron microscopy project (SALVE), enabled by the implementation of a novel spherical and chromatic aberration corrector. *In-situ* observation of dynamic processes in inorganic 2D materials, including crystallization, defect formation and evolution and thermal phase transition is readily achievable (Cao et al., 2020; Kühne et al., 2018; Lehnert et al., 2017). Nonetheless, the structural elucidation of organic 2D materials, e.g., MOFs, remains a challenging task even at unit-cell resolution as radiation damage rapidly evolves during imaging (Egerton, 2019; Kretschmer et al., 2020). The impact of the incident electrons triggers atomic displacement, bond scission, and chemical reactions, leading to the degradation of the structural integrity. Thus, the fast degrading specimen leads to a substantial gap between instrumental resolution and achievable resolution in the recorded HRTEM image.

Atomic displacement due to knock-on damage is often the dominant damage mechanism in inorganic specimens and can be significantly reduced by operating the TEM at an acceleration voltage below the particular knock-on damage threshold (Kaiser et al., 2011; Skowron et al., 2017). The knock-on threshold energy for C-C and C=S bonds is about 85 keV and 140 keV, respectively, which means that when TEM analysis of a specimen containing C-C bonds, the acceleration voltage should be below 85 kV (Chamberlain et al., 2015; Meyer et al., 2012; Skowron et al., 2013), to avert knock-on damage. However, unlike C-C or C=S bonds, which are highly stable under low-voltage electron beams, the likelihood of C-H bond dissociation increases sharply as the electron beam energy decreases below 100 keV (Chamberlain et al., 2015). The instability of C-H bonds against knock-on damage originates mainly from the exceptionally low atomic weight of hydrogen, causing a large amount of energy to be transferred from the incident electrons to hydrogen. The extremely high knock-on damage cross-section of hydrogen (85 barn at 80 kV (Chamberlain et al., 2015)) poses a significant challenge in investigating 2D polymers, 2D c-MOFs and COFs (covalent organic frameworks). Moreover, the removal of hydrogen will create dangling bonds, which further reduces the knock-on threshold of the carbon backbone. Despite the reduced knock-on damage for most other elements by operating the microscope under lower voltages, hydrogen poses a severe limitation on the intrinsic stability of organic specimens during TEM imaging.

Thus, in this work, we utilize a hydrogen-free benzenehexathiol (BHT)-Cu 2D c-MOF - $\text{Cu}_3(\text{BHT})$ - which has the chemical formula $\text{Cu}_3\text{S}_6\text{C}_6$. Through the hydrogen-free structure of the 2D c-MOF, imaging at lower acceleration voltages is enabled. Additionally, the damage resulting from the interactions between beam and specimen electrons is significantly reduced due to the exceptionally high conductivity of $\text{Cu}_3(\text{BHT})$ (2500 S/cm) at room temperature (Egerton, 2012; Huang

et al., 2018). The high electrical conductivity in 2D c-MOFs is achieved through their characteristic strong in-plane π conjugation and out-of-plane interlayer coupling, while (3D) MOFs typically suffer from extremely low electrical conductivity ($<10^{-10} \text{ S cm}^{-1}$). This has opened up an exciting opportunity of not only imaging the 2D c-MOF down to atomic scale at lower voltage (i.e., 80 kV) (Mücke et al., 2024), but also prolonged observation, which enables *in-situ* tracing of the structure, as a much higher electron dose compared to hydrogen-rich (3D) MOF structures can be applied to the specimen before it degrades. The possibility of *in-situ* tracing of the structure led to fascinating research in the field of inorganic specimens (Casu et al., 2018; Storm et al., 2023), inspiring us to explore the effects of the electron beam and external heating on $\text{Cu}_3(\text{BHT})$. In this study, we focus on an *in-situ* investigation of the formation process of copper sulfide nanoparticles resulting from a phase transition in $\text{Cu}_3(\text{BHT})$ at elevated temperatures. To better understand the transition process, three procedures combining heating and electron beam illumination, utilizing 80 kV *in-situ* C_c/C_s corrected HRTEM imaging and *in-situ* heating, are compared. These are either e-beam or heating alone and a combination of both. For the experiment with only heating, HRTEM images were acquired to document the transformation process, but the electron dose was kept as low as possible.

2. Results and discussion

2.1. Synthesis of $\text{Cu}_3(\text{BHT})$

$\text{Cu}_3(\text{BHT})$ crystals were synthesized on the water surface through a three-step process. Initially, a 100 μl chloroform/dimethylformamide solution of BHT (0.3 mg ml^{-1}) was dispersed on the water surface in a 30 cm^2 -sized Teflon trough under ambient conditions (Step 1). Following 30 min of self-assembly and packing of the BHT ligands, a yellow film appeared on the water surface. Subsequently, in step 2, 5 ml of $\text{Cu}(\text{NO}_3)_2$ aqueous solution (1 mg ml^{-1}) was injected into the water subphase to initiate 2D coordination polymerization between Cu^{2+} ions and BHT ligands on the water surface. After 8 h, a black film was formed on the water surface (step 3), which can be transferred horizontally to a Quantifoil TEM grid for TEM characterization. The samples underwent rinsing with chloroform, ethanol, and water, followed by 2 h of drying in ambient conditions before TEM investigations. Fig. 1A presents a low magnification scanning TEM (STEM) high-angle annular dark-field (HAADF) image of the $\text{Cu}_3(\text{BHT})$ 2D c-MOF. The particles demonstrate faceted surface morphology indicating the high crystallinity of the sample.

2.2. Electron resilience of $\text{Cu}_3(\text{BHT})$

The stability of $\text{Cu}_3(\text{BHT})$ was determined by electron dose series in the HRTEM imaging mode (Supplementary Fig. 1). The structural integrity has been monitored as a function of the total accumulated electron dose. With continuous electron bombardment ($2.4 \times 10^3 \text{ e}^-/\text{\AA}^2/\text{s}$), the $\text{Cu}_3(\text{BHT})$ structure started to degrade, which is reflected by the fading of the crystalline reflections in the FFT patterns. The total intensity of the first order reflections was plotted as a function of the accumulated electron dose. As the first order reflection intensity reached 1/e (c.a. 37 %) of the starting intensity, the accumulated dose is defined as the critical dose. Remarkably, the critical dose of $\text{Cu}_3(\text{BHT})$ shows an extremely high value of around $(1.73 \pm 0.14) \times 10^5 \text{ e}^-/\text{\AA}^2$ at 80 kV (SALVE instrument) and $(2.48 \pm 0.77) \times 10^5 \text{ e}^-/\text{\AA}^2$ at 300 kV (Mücke et al., 2024) (TITAN instrument), which is about five orders of magnitude higher than the critical dose of typical MOF structures, such as UiO-66 and ZIF-8, where this value is smaller than $20 \text{ e}^-/\text{\AA}^2$ (Zhang et al., 2018), and is comparable to the electron resilience of inorganic 2D materials (Algara-Siller et al., 2013). It should be noted that the critical dose at 80 kV and 300 kV are of the same order of magnitude, allowing for the use of enhanced contrast at 80 kV without compromising image

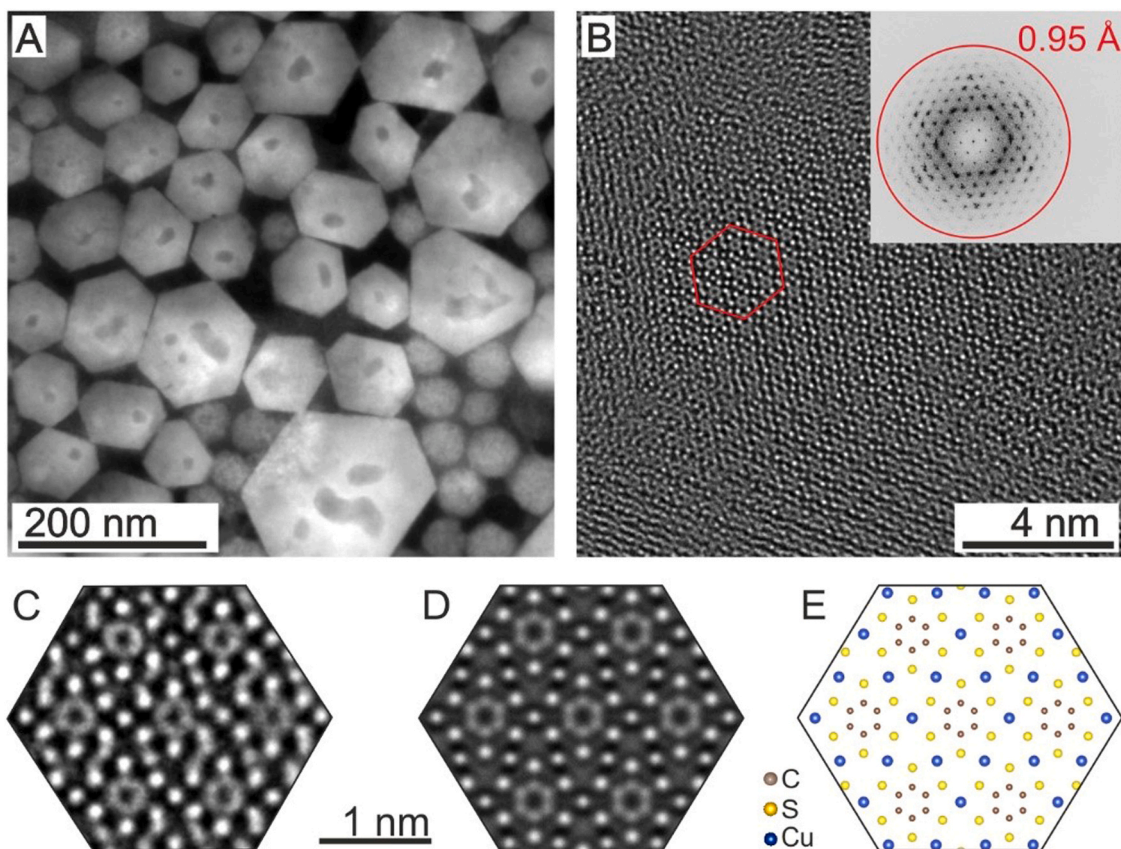


Fig. 1. Imaging $\text{Cu}_3(\text{BHT})$ (A) STEM HAADF image of the $\text{Cu}_3(\text{BHT})$ crystals, showing clear hexagonal facets. (B) 80 kV Cc/Cs-corrected HRTEM image of a thin area of the $\text{Cu}_3(\text{BHT})$ particle obtained with an electron dose of $5200 \text{ e}^-/\text{\AA}^2$. All atomic columns have been clearly resolved. Inset: corresponding FFT pattern demonstrating an imaging resolution of 0.95 \AA . (C) Magnified image of the red area in B, (D) image simulation of a $\text{Cu}_3(\text{BHT})$ particle, (E) atomic model of $\text{Cu}_3(\text{BHT})$.

quality.

2.3. Cc/Cs-corrected-HRTEM imaging of $\text{Cu}_3(\text{BHT})$ and chemical analysis

We use the Cc/Cs-corrected SALVE (Sub-Angstrom Low-Voltage Electron Microscopy) instrument operated at 80 kV in HRTEM imaging mode. Fig. 1B displays the corresponding HRTEM image of $\text{Cu}_3(\text{BHT})$ showcasing an image resolution of 0.95 \AA (for further insights see (Mücke et al., 2024)). A qualitative comparison of the simulated HRTEM image contrast (Fig. 1D), based on the structural model depicted in Fig. 1E, with the experimental image (Fig. 1C) shows good agreement. Additionally, all atomic columns are clearly resolved. The achievement of sub-angstrom resolution at 80 kV has been enabled by the high electron resilience through the hydrogen-free design of the structure and the high electrical conductivity.

To further investigate the chemical composition of the $\text{Cu}_3(\text{BHT})$ 2D c-MOF, STEM energy-dispersive X-ray mapping was conducted. As shown in Supplementary Fig. 2, Cu: S ratio was determined to be $1: 2.1 \pm 0.15$, whereas the theoretical value is $1: 2$ (chemical formula: $\text{Cu}_3\text{S}_6\text{C}_6$). The good agreement between the measured and theoretical Cu: S ratio further confirms the successful synthesis of $\text{Cu}_3(\text{BHT})$ with the expected structure and chemical composition.

In *in-situ* heating TEM experiments using a MEMS chip, energy is transferred to the specimen through both, the electron beam and external heat. Previous studies have demonstrated that both forms of energy transfer can induce phase transitions (Storm et al., 2023). However, the effect of simultaneously applying external heat and electron beam illumination may alter the transition temperature (Casu et al., 2018). This effect has not been studied thoroughly. Therefore, this paper

explores how energy transfer via the electron beam and external heat affects the $\text{Cu}_3(\text{BHT})$ 2D c-MOF, both separately and in combination.

Firstly, we investigate the effect of the 80 kV electron beam illumination on $\text{Cu}_3(\text{BHT})$ flakes with a continuous dose rate of $2.4 \times 10^3 \text{ e}^-/\text{\AA}^2\text{s}$. Fig. 2 A-C show three snapshots, depicting the same sample area with increasing accumulated electron dose. As seen, the crystallinity of the c-MOF gradually diminishes with growing accumulated electron dose, as seen in the FFT shown in the insets. It is apparent from this observation that solely illuminating the $\text{Cu}_3(\text{BHT})$ leads to sample degradation.

Secondly, we investigate the combined effect of the 80 kV electron beam together with external heating. A MEMS heating holder was employed to monitor the effects of heating on the specimen *in-situ*. Fig. 3A shows Cc/Cs-corrected HRTEM images of $\text{Cu}_3(\text{BHT})$ at $460 \text{ }^\circ\text{C}$. The corresponding FFT reveals a hexagonal pattern with first-order reflections at 1.4 nm^{-1} , consistent with the pristine c-MOF structure. Upon heating to $480 \text{ }^\circ\text{C}$ (Fig. 3B), the c-MOF reflections start to vanish, indicating structural decomposition. Concurrently, new reflections emerge at 3.1 nm^{-1} . At $510 \text{ }^\circ\text{C}$, the original c-MOF reflections vanish entirely. Remaining are first and second-order reflections at 3.1 nm^{-1} and 5.1 nm^{-1} , respectively indicating the formation of a new crystalline phase with hexagonal symmetry. Interestingly, the 100 reflections of the new crystal phase align with the 110 reflections of $\text{Cu}_3(\text{BHT})$ (Fig. 4A and B), resulting in a 30° rotation between the two hexagonal unit cells. This transition was also reproduced with an acceleration voltage of 200 kV.

Thirdly, we investigated the effect of heating with minimization of the electron beam effect. For this, the electron beam was blanked during the heating process, and only several snapshots were captured at specific temperature intervals, to minimize the applied electron dose.

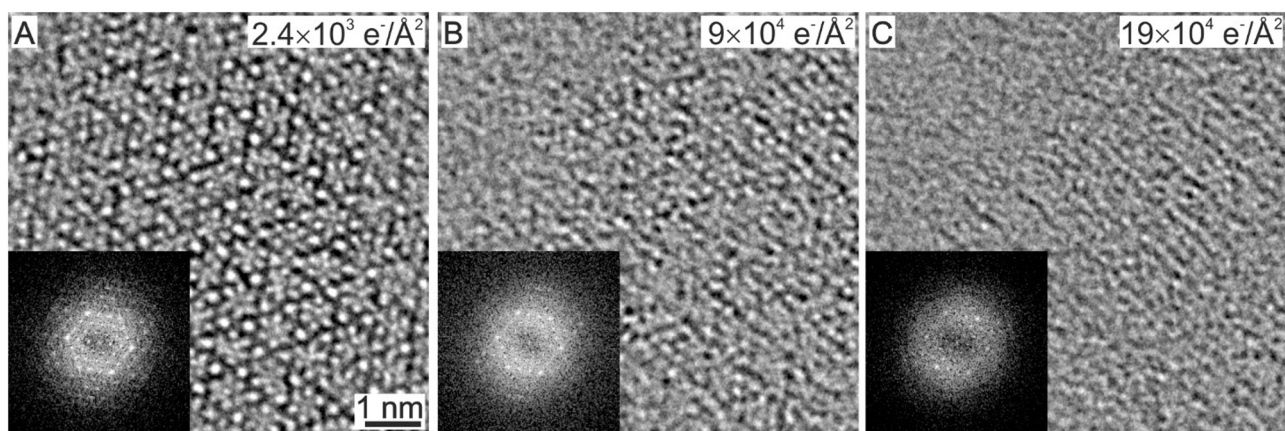


Fig. 2. MOF degradation through electron beam imaging. (A-C) 80 kV Cc/Cs-corrected HRTEM image of a $\text{Cu}_3(\text{BHT})$ crystal, in [001] direction, with growing accumulated electron dose from $2.4 \times 10^3 \text{ e}^-/\text{\AA}^2$ to $19 \times 10^4 \text{ e}^-/\text{\AA}^2$. In the inset the corresponding FFT patterns are displayed, in (A) the 100 reflections at 1.4 nm^{-1} is marked in red. As seen, with growing accumulated electron dose the crystalline phase gets damaged and no new phase is emerging.

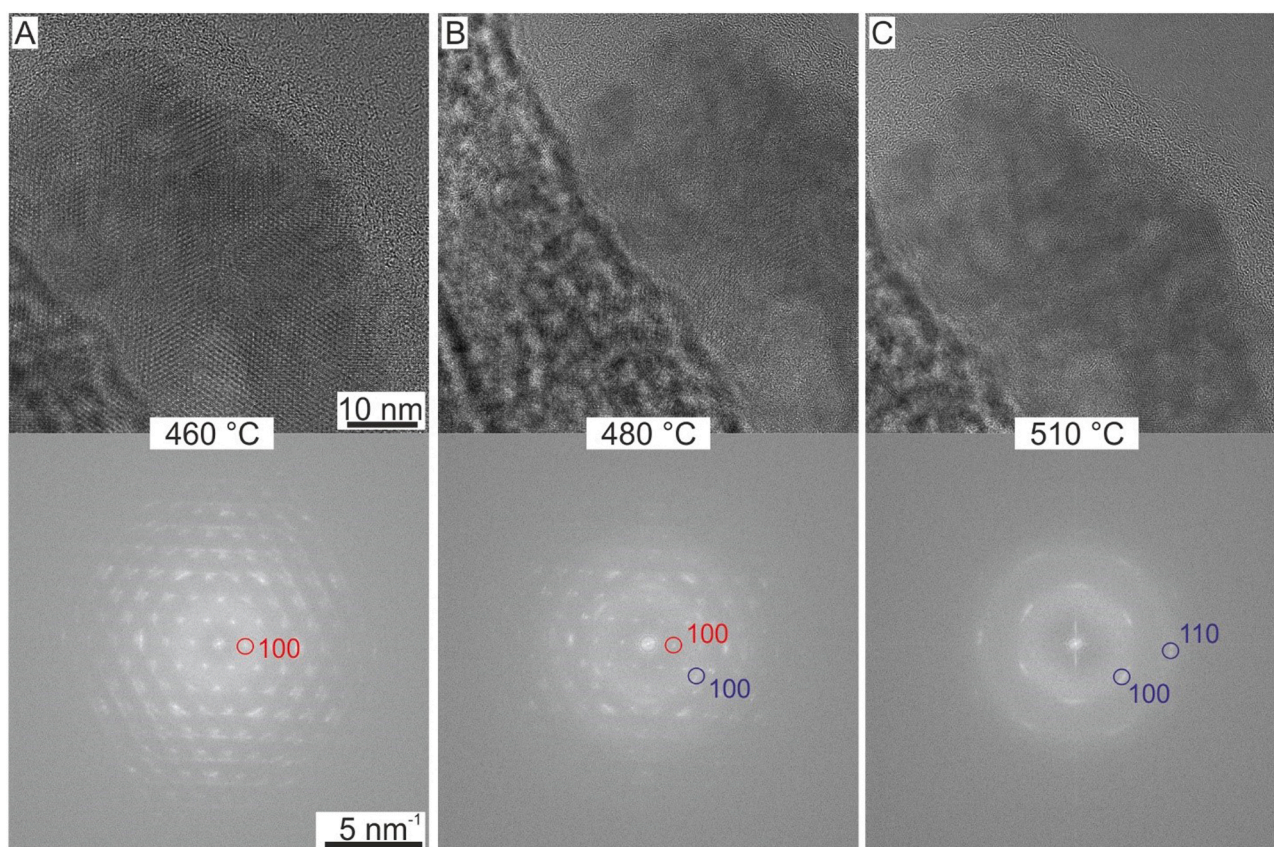


Fig. 3. In-situ heating of $\text{Cu}_3(\text{BHT})$. (A-C) Cc/Cs-corrected HRTEM images of $\text{Cu}_3(\text{BHT})$ particles at increasing temperature from $460 \text{ }^\circ\text{C}$ to $510 \text{ }^\circ\text{C}$ (as indicated) and corresponding FFT patterns. Images obtained with a dose rate of $1.2 \times 10^3 \text{ e}^-/\text{\AA}^2\text{s}$, and 1 s exposure time. In (A) the 100 reflections (red) at 1.4 nm^{-1} are in perfect agreement with the first order reflection of the calculated $\text{Cu}_3(\text{BHT})$ structure. Upon heating, new reflections (blue) at 3.1 nm^{-1} and 5.1 nm^{-1} begin to emerge, while the $\text{Cu}_3(\text{BHT})$ reflections are fading.

[Supplementary Fig. S5](#) presents three TEM images taken at 600 , 620 and $640 \text{ }^\circ\text{C}$ and their corresponding FFTs. In the FFT patterns, we observed the same reflections at 3.1 nm^{-1} , albeit at about $140 \text{ }^\circ\text{C}$ higher transition temperature of approximately $620 \text{ }^\circ\text{C}$. This behavior can be explained through additional energy deposited by inelastic interactions of the electron beam with the specimen (Egerton et al., 2004).

To further elucidate the structure of the new crystalline phase, we conducted EDX mapping. As shown in [Supplementary Fig. S3](#), after heating to $600 \text{ }^\circ\text{C}$, the c-MOF reflections have entirely disappeared in the

selected-area electron diffraction pattern, leaving only two rings at 3.1 nm^{-1} and 5.1 nm^{-1} , demonstrating the completion of the phase transition. The EDX results revealed a Cu: S ratio of $1: 0.83 \pm 0.26$, suggesting the formation of CuS. Moreover, the lattice spacing and symmetry closely correspond to copper monosulfide viewed in [001] projection (Liu et al., 2017) ([Supplementary Fig. S4](#)).

[Fig. 4A](#) and [C](#) show the $\text{Cu}_3(\text{BHT})$ and CuS FFT pattern along the [001] direction. In [Fig. 4B](#) both patterns are overlaid, demonstrating a 30° rotation between the structures. Initially, it is puzzling how CuS

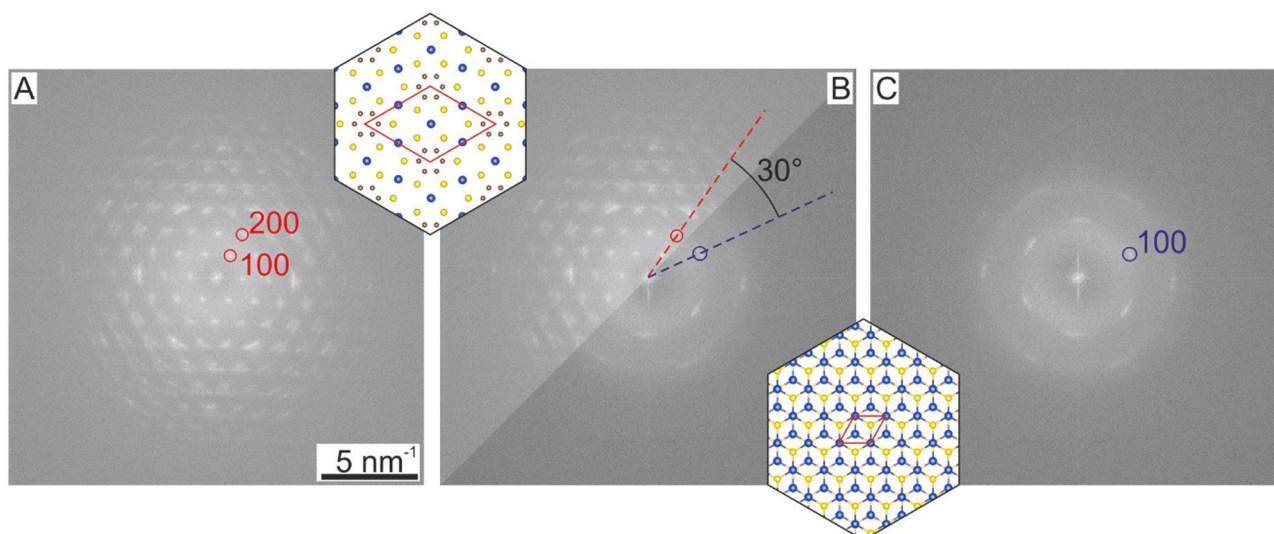


Fig. 4. $\text{Cu}_3(\text{BHT})$ -to- CuS transition and crystallographic orientation. (A, C) FFT patterns of $\text{Cu}_3(\text{BHT})$ and CuS obtained from the same sample area before and after the phase transition. In (A), the 100 and 200 reflections of $\text{Cu}_3(\text{BHT})$ are marked, in (C) the 100 reflection of CuS are marked in blue. In (B) the FFT patterns from (A) and (C) are overlaid and the 200 reflection of $\text{Cu}_3(\text{BHT})$ (red) and the 100 reflection of CuS (blue) are highlighted again. By comparing both reflections, a clear rotation of 30° between both lattices can be seen. Upper inset: atomic structure model of $\text{Cu}_3(\text{BHT})$; Lower inset: atomic structure model of two-layer CuS . Unit cells marked by red diamond.

could form on the c-MOF layers, given the lack of clear overlap in atomic positions (compare insets of Fig. 4). The unit cell parameters of both materials suggest a mismatch of 10 %, when using a supercell consisting of 1 $\text{Cu}_3(\text{BHT})$ and 2 and 4 CuS unit cells along the vertical and horizontal directions (with respect to the CuS reflections), respectively. However, through the 30° rotation, this lattice mismatch is drastically reduced: In the horizontal direction the lattice mismatch between 1 $\text{Cu}_3(\text{BHT})$ and 4 CuS cells is reduced to 4 %, while in the vertical direction, a supercell of 2 $\text{Cu}_3(\text{BHT})$ and 5 CuS cells reduces the mismatch to 2 %. Based on this information, we propose that the structural transition occurred through the diffusion and recrystallization of Cu and S, with the pristine c-MOF acting as an epitaxial substrate for the growth of CuS . This hypothesis is further supported by the observation that the CuS crystals only grow directly on the remnants of the c-MOF particle and not, for example, adjacent to the particle on the supporting film (see Supplementary Fig. 6).

3. Conclusion and outlook

We demonstrated that the crystalline, hydrogen-free and conductive $\text{Cu}_3(\text{BHT})$ 2D c-MOF allows for *in-situ* 80 kV C_c/C_s -corrected HRTEM imaging. Upon exposure to a high electron dose of $1.7 \times 10^5 \text{ e}^-/\text{\AA}^2$, $\text{Cu}_3(\text{BHT})$ undergoes a transition from a crystalline to an amorphous phase. However, upon heating, we observed a phase transformation of the crystalline $\text{Cu}_3(\text{BHT})$ into a new crystalline phase, identified as CuS by HRTEM and EDX mapping. The phase transition temperature ranges from 480°C to 620°C , with a tendency towards the lower end under continuous electron beam illumination and towards the higher end when the sample is only heated. This finding reveals a method to engineer the phase transition temperature of this material. The CuS nanoparticles exhibit a well-defined crystallographic orientation relationship (30° rotation of the unit cells) to the $\text{Cu}_3(\text{BHT})$ host crystal, indicating that diffusion and recrystallization of Cu and S occur on the $\text{Cu}_3(\text{BHT})$ surface, acting as an epitaxial substrate. This implies that the size and structure of the newly formed crystal is influenced by the size and structure of the host c-MOF crystal.

Thus, we have demonstrated a controlled pathway for the formation of crystalline nanoparticles via c-MOF-to-nanoparticle transitions. By varying the MOF crystal precursor, we can influence the size of the resulting CuS particle and, consequently, their properties. Additionally,

by adjusting the electron irradiation, the transition temperature can be altered. This detailed understanding of the transformation process may pave the way for further experimental and theoretical studies aimed at highly controlled nanoparticle formation, which may include the production of CuO and NiS from 2D c-MOFs $\text{Cu}_3(\text{HHB})$ and $\text{Ni}_3(\text{BHT})$, respectively.

4. Methods

Transmission electron microscopy. HRTEM combined with *in-situ* heating experiments were performed on the image-side C_c/C_s aberration-corrected SALVE (Sub-Angstrom Low-Voltage Electron Microscopy) instrument operated at 80 kV. At this voltage, the instrumental resolution is 76 pm. The SALVE instrument is hosted in a FEI Titan Themis³ column and equipped with a CEOS aberration corrector that corrects for first-order chromatic aberrations, axial geometric aberrations up to including the fifth order, and off-axial geometric aberrations. The TEM is equipped with a FEI CETA 16 M fiber-coupled CMOS camera. STEM HAADF imaging and EDX mapping were performed on a Thermo Fisher Talos F200X (with SuperX) operated at an acceleration voltage of 80 kV.

In-situ heating experiments. Heating experiments were performed on FEI MEMS chips on a FEI Nano-Ex/iV heating holder. The MEMS chips consist of 22 viewing windows covered with a 15-nm-thick holey SiN_x membrane. The MEMS chip was heated up to 700°C .

Funding

D.M., B.L., H.Q., and U.K. gratefully acknowledge the funding from the Germany Research Foundation (DFG) (Grant No. 492191310, 426572620, 417590517 (SFB 1415)). Z.W., R.D., and X.F. acknowledge the financial support from ERC starting grant (FC2DMOF, grant no. 852909), ERC Consolidator Grant (T2DCP), DFG project (2D polyanilines, no. 426572620), GRK2861 (no. 491865171), CRC 1415 (Chemistry of Synthetic Two-Dimensional Materials, no. 417590517).

Author statement

D.M., B.L. and H.Q. performed the TEM experiments under the guidance of U.K.. D.M. and H.Q. conceived and designed the TEM

experiments. D. M., B. L., H. Q. and U.K. analyzed and/or discussed the TEM data. Z.W., R.D., and X.F. synthesized the MOFs. D.M., H.Q. and U. K. wrote the manuscript. All authors commented on the manuscript.

Declaration of Competing Interest

The authors declare that they have no known competing financial interests or personal relationships that could have appeared to influence the work reported in this paper.

Data availability

Data will be made available on request. All data supporting the findings of this study are available within the paper and its supplementary materials. Additional data related to this paper may be requested from the corresponding authors.

Appendix A. Supporting information

Supplementary data associated with this article can be found in the online version at doi:10.1016/j.micron.2024.103677.

References

- Algara-Siller, G., Kurasch, S., Sedighi, M., Lehtinen, O., Kaiser, U., 2013. The pristine atomic structure of MoS₂ monolayer protected from electron radiation damage by graphene. *Appl. Phys. Lett.* 103, 203107.
- Cao, K., Biskupek, J., Stoppio, C.T., McSweeney, R.L., Chamberlain, T.W., Liu, Z., Suenaga, K., Skowron, S.T., Besley, E., Khlobystov, A.N., Kaiser, U., 2020. Atomic mechanism of metal crystal nucleus formation in a single-walled carbon nanotube. *Nat. Chem.* 12, 921–928. <https://doi.org/10.1038/s41557-020-0538-9>.
- Casu, A., Lambertini, A., Stassi, S., Falqui, A., 2018. Crystallization of TiO₂ nanotubes by in situ heating TEM. *Nanomaterials*. <https://doi.org/10.3390/nano8010040>.
- Chamberlain, T.W., Biskupek, J., Skowron, S.T., Bayliss, P.A., Bichoutskaia, E., Kaiser, U., Khlobystov, A.N., 2015. Isotope substitution extends the lifetime of organic molecules in transmission electron microscopy. *small* 11, 622–629. <https://doi.org/10.1002/sml.201402081>.
- Chen, L., Shen, Y., Bai, J., Wang, C., 2009. Novel symmetrical coraloid Cu 3D superstructures: solid-state synthesis from a Cu-carboxylate MOF and their in-situ thermal conversion. *J. Solid State Chem.* 182, 2298–2306. <https://doi.org/10.1016/j.jssc.2009.06.007>.
- Corma, A., García, H., Llabrés i Xamena, F.X., 2010. Engineering metal organic frameworks for heterogeneous catalysis. *Chem. Rev.* 110, 4606–4655. <https://doi.org/10.1021/cr9003924>.
- Dong, R., Zhang, Zhitao, Tranca, D.C., Zhou, S., Wang, M., Adler, P., Liao, Z., Liu, F., Sun, Y., Shi, W., Zhang, Zhe, Zschech, E., Mannsfeld, S.C.B., Felser, C., Feng, X., 2018. A coronene-based semiconducting two-dimensional metal-organic framework with ferromagnetic behavior. *Nat. Commun.* 9, 2637. <https://doi.org/10.1038/s41467-018-05141-4>.
- Egerton, R.F., 2012. Mechanisms of radiation damage in beam-sensitive specimens, for TEM accelerating voltages between 10 and 300 kV. *Microsc. Res. Tech.* 75, 1550–1556. <https://doi.org/10.1002/jemt.22099>.
- Egerton, R.F., 2019. Radiation damage to organic and inorganic specimens in the TEM. *Micron* 119, 72–87. <https://doi.org/10.1016/j.micron.2019.01.005>.
- Egerton, R.F., Li, P., Malac, M., 2004. Radiation damage in the TEM and SEM. *Micron* 35, 399–409. <https://doi.org/10.1016/j.micron.2004.02.003>.
- Goel, S., Chen, F., Cai, W., 2014. Synthesis and biomedical applications of copper sulfide nanoparticles: from sensors to theranostics. *Small* 10, 631–645. <https://doi.org/10.1002/sml.201301174>.
- Haider, M., Uhlemann, S., Schwan, E., Rose, H., Kabius, B., Urban, K., 1998. Electron microscopy image enhanced. *Nature* 392, 768–769. <https://doi.org/10.1038/33823>.
- Huang, X., Sheng, P., Tu, Z., Zhang, F., Wang, J., Geng, H., Zou, Y., Di, C., Yi, Y., Sun, Y., Xu, W., Zhu, D., 2015. A two-dimensional π -d conjugated coordination polymer with extremely high electrical conductivity and ambipolar transport behaviour. *Nat. Commun.* 6, 7408. <https://doi.org/10.1038/ncomms8408>.
- Huang, X., Zhang, S., Liu, L., Yu, L., Chen, G., Xu, W., Zhu, D., 2018. Superconductivity in a Copper(II)-based coordination polymer with perfect kagome structure. *Angew. Chem. Int. Ed.* 57, 146–150. <https://doi.org/10.1002/anie.201707568>.
- Jia, C.L., Mi, S.B., Barthel, J., Wang, D.W., Dunin-Borkowski, R.E., Urban, K.W., Thust, A., 2014. Determination of the 3D shape of a nanoscale crystal with atomic resolution from a single image. *Nat. Mater.* 13, 1044–1049.
- Kaiser, U., (www.salve-project.de), 06.2024.
- Kaiser, U., Biskupek, J., Meyer, J.C., Leschner, J., Lechner, L., Rose, H., Stöger-Pollach, M., Khlobystov, A.N., Hartel, P., Müller, H., Haider, M., Eyhusen, S., Benner, G., 2011. Transmission electron microscopy at 20 kV for imaging and spectroscopy. *Ultramicroscopy* 111, 1239–1246. <https://doi.org/10.1016/j.ultramic.2011.03.012>.
- Kretschmer, S., Lehnert, T., Kaiser, U., Krashennnikov, A.V., 2020. Formation of defects in two-dimensional MoS₂ in the transmission electron microscope at electron energies below the knock-on threshold: the role of electronic excitations. *Nano Lett.* 20, 2865–2870.
- Kühne, M., Börrnert, F., Fecher, S., Ghorbani-Asl, M., Biskupek, J., Samuëlis, D., Krashennnikov, A.V., Kaiser, U., Smet, J.H., 2018. Reversible superdense ordering of lithium between two graphene sheets. *Nature* 564, 234–239. <https://doi.org/10.1038/s41586-018-0754-2>.
- Lehnert, T., Kinyanjui, M.K., Ladenburger, A., Rommel, D., Wörle, K., Börrnert, F., Leopold, K., Kaiser, U., 2017. In Situ crystallization of the insoluble anhydrite All phase in graphene pockets. *ACS Nano* 11, 7967–7973. <https://doi.org/10.1021/acsnano.7b02513>.
- Li, J.-R., Sculley, J., Zhou, H.-C., 2012. Metal-organic frameworks for separations. *Chem. Rev.* 112, 869–932. <https://doi.org/10.1021/cr200190s>.
- Linck, M., Hartel, P., Uhlemann, S., Kahl, F., Müller, H., Zach, J., Haider, M., Niestadt, M., Bischoff, M., Biskupek, J., Lee, Z., Lehnert, T., Börrnert, F., Rose, H., Kaiser, U., 2016. Chromatic aberration correction for atomic resolution TEM imaging from 20 to 80 kV. *Phys. Rev. Lett.* 117, 76101. <https://doi.org/10.1103/PhysRevLett.117.076101>.
- Liu, Y., Liu, M., Swihart, M.T., 2017. Reversible crystal phase interconversion between covellite CuS and high chalcocite Cu₂S nanocrystals. *Chem. Mater.* 29, 4783–4791. <https://doi.org/10.1021/acs.chemmater.7b00579>.
- Luo, L., Wang, Y., Huo, S., Lv, P., Fang, J., Yang, Y., Fei, B., 2019. Cu-MOF assisted synthesis of CuS/Cds(H)/Cds(C): enhanced photocatalytic hydrogen production under visible light. *Int. J. Hydrog. Energy* 44, 30965–30973. <https://doi.org/10.1016/j.ijhydene.2019.09.136>.
- Meyer, J.C., Eder, F., Kurasch, S., Skakalova, V., Kotakoski, J., Park, H.J., Roth, S., Chuvilil, A., Eyhusen, S., Benner, G., Krashennnikov, A.V., Kaiser, U., 2012. Accurate measurement of electron beam induced displacement cross sections for single-layer graphene. *Phys. Rev. Lett.* 108, 1–6. <https://doi.org/10.1103/PhysRevLett.108.196102>.
- Mücke, D., Cooley, L., Liang, B., Wang, Z., Park, S., Dong, R., Feng, X., Qi, H., Besley, E., Kaiser, U., 2024. Understanding the electron beam resilience of two-dimensional conjugated metal-organic frameworks. *Nano Lett.* <https://doi.org/10.1021/acs.nanolett.3c04125>.
- Murray, L.J., Dincă, M., Long, J.R., 2009. Hydrogen storage in metal-organic frameworks. *Chem. Soc. Rev.* 38, 1294–1314. <https://doi.org/10.1039/B802256A>.
- Negar, M.K., Morvarid, R., Sima, T.D., Masoumeh, Y., 2021. Synthesis and characterization of bismuth oxide nanoparticle by thermal decomposition of bismuth-based MOF and evaluation of its Nanocomposite. *Iran. J. Chem. Chem. Eng.* 40, 11–19. <https://doi.org/10.30492/ijcce.2019.37263>.
- Saranya, M., Santhosh, C., Augustine, S.P., Grace, A.N., 2014. Synthesis and characterization of CuS nanomaterials using hydrothermal route. *J. Exp. Nanosci.* 9, 329–336. <https://doi.org/10.1080/17458080.2012.661471>.
- Shahangi Shirazi, F., Akhbari, K., 2015. Preparation of zinc oxide nanoparticles from nanoporous metal-organic framework with one-dimensional channels occupied with guest water molecules. *Inorg. Chim. Acta* 436, 1–6. <https://doi.org/10.1016/j.ica.2015.07.025>.
- Skowron, S.T., Chamberlain, T.W., Biskupek, J., Kaiser, U., Besley, E., Khlobystov, A.N., 2017. Chemical reactions of molecules promoted and simultaneously imaged by the electron beam in transmission electron microscopy. *Acc. Chem. Res.* 50, 1797–1807. <https://doi.org/10.1021/acs.accounts.7b00078>.
- Skowron, S.T., Lebedeva, I.V., Popov, A.M., Bichoutskaia, E., 2013. Approaches to modelling irradiation-induced processes in transmission electron microscopy. *Nanoscale* 5, 6677–6692. <https://doi.org/10.1039/C3NR02130K>.
- Storm, A., Köster, J., Ghorbani-Asl, M., Kretschmer, S., Gorelik, T.E., Kinyanjui, M.K., Krashennnikov, A.V., Kaiser, U., 2023. Electron-Beam- and thermal-annealing-induced structural transformations in few-layer MnPS₃. *ACS Nano* 17, 4250–4260. <https://doi.org/10.1021/acsnano.2c05895>.
- Widmer, R.N., Lampronti, G.L., Anzellini, S., Gaillac, R., Farsang, S., Zhou, C., Belenguer, A.M., Wilson, C.W., Palmer, H., Kleppe, A.K., Wharmby, M.T., Yu, X., Cohen, S.M., Telfer, S.G., Redfern, S.A.T., Coudert, F.-X., MacLeod, S.G., Bennett, T. D., 2019. Pressure promoted low-temperature melting of metal-organic frameworks. *Nat. Mater.* 18, 370–376. <https://doi.org/10.1038/s41563-019-0317-4>.
- Zhang, L., Hu, Y.H., 2010. A systematic investigation of decomposition of nano Zn₄O(C₈H₄O₄)₃ metal-organic framework. *J. Phys. Chem. C* 114, 2566–2572. <https://doi.org/10.1021/jp911043r>.
- Zhang, D., Zhu, Y., Ying, X., Hsiung, C., Sougrat, R., Li, K., Han, Y., 2018. Atomic-resolution transmission electron microscopy of electron beam-sensitive crystalline materials. *Science* 679, 675–679.